

# Aerodynamic Design of Turbomachinery Cascades Using an Enhanced Time-Marching Finite Volume Method

J. C. Páscoa<sup>1</sup>, A. C. Mendes<sup>1</sup>, L. M. C. Gato<sup>2</sup>, R. Elder<sup>3</sup>

**Abstract:** The paper presents an aerodynamic design method for turbomachinery cascades of blades. The prescribed conditions are the aerodynamic blade load and the blade thickness distributions. An iterative procedure was implemented, based on the solution of the Euler equations, to seek the blade geometry that provides the specified design conditions. A central finite-volume explicit time-marching scheme is used to solve the Euler equations in two-dimensional flow. The numerical scheme uses an adaptive nonlinear artificial dissipation term based on the limiter theory. Starting with the results from the flow analysis through an initially guessed cascade geometry, the design code modifies the blade camber line by relating the axial distribution of the mean tangential velocity component through the cascade with the blade camber-line angle. The procedure allows the iterative calculation of the blade geometry that gives the desired aerodynamic blade load distribution. The accuracy of the method has been verified by calculating a parabolic cascade and by redesigning a transonic compressor cascade.

**keyword:** inverse method, time-marching, finite volume.

## 1 Introduction

Modern turbomachinery design processes do not simply seek the efficiency increase of the devices. They are also conceived to minimize human interaction and, in this manner, reduce design errors and costs. By using automatic design methods the designer prescribes certain desired conditions for the flow domain, whereas the method provides the blade geometry. Some of these techniques

are nowadays used in industry for turbomachinery design. However, they still require more development studies in order to reduce human involvement [Pierret and van den Braembussche (1998)].

Among the possible automatic design approaches, some authors couple flow-analysis tools to optimization methods and artificial neural networks. This mimics the trial and error process of the human iterative design [Köller, Mönig, Küsters, and Schreiber (2000); Burguburu, Toussaint, Bonhomme, and Leroy (2004)]. The goal of an optimization method is to find the geometry that minimizes the objective function, the blade performance being evaluated with an analysis code, see [Okumura and Kawahara (2000)]. Besides, in three-dimensional flow the control over the flowfield imposed by the constraints on the blade surface and side walls seems more efficiently tractable by other inverse design approaches. This is due to possible difficulties in specifying the objective function and because optimization methods have been found to require very large computational times. Recent results from Levin and Shyy (2001) demonstrate that typical optimizations, based on the response surface method, may require as much as 250 flowfield analysis. Their solutions were based on an inviscid/viscous procedure that couples a panel method code and a boundary layer integral method. Moreover, this class of methods is very prone to find local (instead of global) minima for the objective function. Optimization techniques coupled to finite-volume codes, solving either the Euler or the Navier-Stokes equations, are feasible but take large computational time for routine design tasks. Consequently, fast, robust and versatile inverse methods are required, with potential for extension to three-dimensional flow. Nevertheless, optimization techniques can eventually be coupled to other type of inverse methods in order to optimize the imposed flow conditions. This approach might diminish the computational load as compared to those of the pure optimization methods.

<sup>1</sup>Department of Electromechanical Engineering, Universidade da Beira Interior, Covilhã, Portugal.

<sup>2</sup>Department of Mechanical Engineering, Instituto Superior Técnico, Technical University of Lisbon, Lisbon, Portugal.

<sup>3</sup>Department of Aeronautic and Automotive Engineering, Loughborough University, Loughborough, United Kingdom.

Earlier inverse methods were based on potential flow models considering either analytical or numerical approaches, see [Lewis (1982); Borges (1990)]. Later, due to the increasing availability of computer resources, methods were developed that manage to handle rotational flows with shock waves, by solving the Euler system of equations [Nicke, Steinert, Weber, and Starcken (1993); Dang and Isgro (1995); Borges, Gato, and Pereira (1996)]. Usually the equations are solved in a numerical domain which changes during the calculation, since the blade geometry is part of the solution of the problem. Therefore, the method is iterative and a first guess of the geometry is needed to initiate the calculation. A purely mathematical algorithm performs the modification of the geometry, by minimizing an error function that expresses the difference between the desired and the actual blade pressure distributions. In some two-dimensional blade-to-blade inverse methods, the usual choice for prescribing the flow conditions is the pressure distribution over the blade pressure and suction surfaces. The specification of the pressure distribution is usually selected because it makes it easier to avoid flow separation in design conditions, by controlling the pressure gradient along the blade surface. This design philosophy is easily applicable in two-dimensional flow, because the streamlines are known to lie in the plane under consideration. In a truly three-dimensional design, the prescription of velocity or pressure on both blade surfaces may lose its advantage since the stream surface twist is not known in advance. Furthermore Demeulenaere and van den Braembussche (1998) reported some difficulties when defining target pressure distributions to design blade shapes respecting thickness requirements. Recently, they considered a different strategy that combines aerodynamic and structural design. This strategy was implemented by prescribing the blade thickness distribution and the static pressure either on the suction side or on the pressure side. This resulted in some loss of aerodynamic efficiency but allowed the design of blades with realistic thickness distributions, particularly near the trailing edge.

In order to circumvent some of the limitations referred to above, as design variables we use the mean tangential velocity distribution  $\bar{V}_y(x)$  along the cascade and the blade thickness distribution [Borges, Gato, and Pereira (1996)]. An immediate consequence of this choice is that the designer no longer has direct control over the stream-

wise velocity distribution or the pressure distribution on the blade surface. However, this drawback is compensated in a number of ways. First of all, the prescription of a convenient thickness distribution ensures that a realistic blade shape will always be obtained. Also, since the blade stress is directly related to the blade thickness, the ability to prescribe the thickness allows the designer to take the stress issue into account before starting the aerodynamic design. This saves a large amount of time in the iteration between the aerodynamic and the structural design. Indeed, it is envisaged to strengthen the link between these two design criteria by coupling the present inverse aerodynamic design method with a fluid-structure analysis code [Rugonyi and Bathe (2001)]. Secondly, specifying the blade pressure load, instead of the velocity or the pressure distribution on both surfaces, greatly eases the constraints imposed by the existence problem. Actually there is no closed solution for this problem in compressible flow, but we may drain some insights to this class of flow from the work of Volpe and Melnik (1981). More recently, numerical experiments presented in [Páscoa, Mendes, and Gato (2004)] gave evidence that most of the designs with arbitrarily specified blade loading distributions have solution. Consequently, this design strategy seems more robust than those for which the variables are specified on both blade surfaces, see also [Dang (1995)]. One of the drawbacks of the latter methodology is that a dozen of flow analysis cycles are typically needed in order to reach convergence, an issue that requires further attention. In order to reduce computational costs a novel class of methods, called Meshless Local Petrov-Galerkin (MLPG) methods could be used, see [Atluri and Zhu (1998)]. Particularly the MLPG5 method, which uses meshless trial functions and a Heaviside function in overlapping subdomains, can be considered as a Meshless Finite Volume Method, see [Atluri and Shen (2002)]. The use of such methods may contribute for a better description of the flow through cascades of blades of complex geometry and for an efficient treatment of shock wave discontinuities, for instance by means of grid adaptation.

Nevertheless, the present method is foreseen to be straightforwardly extensible to the design of three-dimensional geometries. Moreover, this method is easily applicable to treat viscous flows [Demeulenaere, Leonard, and van den Braembussche (1997)], in contrast with other design methods that modify the blade bound-

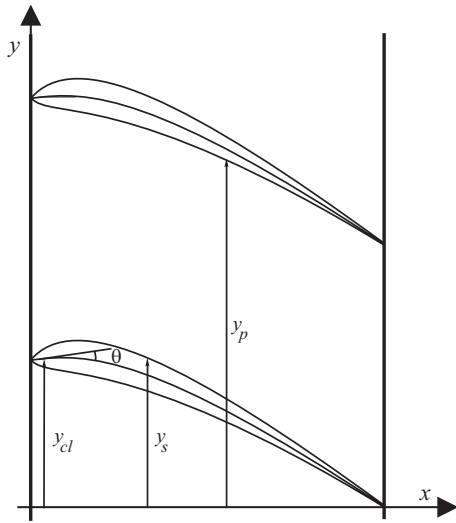


**Figure 1** : Rectilinear cascade of blades.

ary conditions during the calculations in order to achieve faster convergence rates. In the present implementation, a robust Euler code enabled the use of the flowfield results from the previous design iteration as the initial condition for the following flow analysis. The computed numerical results showed that a substantial reduction of the computational time has been accomplished with this methodology.

## 2 Inverse design formulation

Here we briefly explain the inverse design method based on the iterative analysis procedure of Borges, Gato, and Pereira (1996). The differences between that method and the implementation presented here are emphasized. The design methodology uses the information obtained by the iterative flowfield analysis, see Fig. 1. The direct analysis program is based on the time-marching algorithm described in section 3. The design method assumes that the prescribed mean tangential velocity component along the cascade is a function of the blade camber-line angle. Therefore, the design method modifies the blade camber line while the computed mean tangential velocity is converging to the one prescribed as input. We note that the blade thickness distribution is also given as input.

The mean tangential velocity distribution  $\bar{V}_y(x)$  along the cascade is chosen as a design variable. This is directly related to the flow-produced force on the blade. By performing a momentum balance along the direction  $y$ ,

Fig. 1, Borges, Gato, and Pereira (1996) have shown that the following relation exists between the aerodynamic blade load distribution (pressure difference,  $\Delta p$ , between the blade suction and pressure surfaces) and the derivative of the mean tangential velocity component

$$-\frac{d}{dx} \left[ \frac{\int_{y_s}^{y_p} \rho V_x V_y dy}{\int_{y_s}^{y_p} \rho V_x dy} \right] = \frac{\Delta p}{\dot{m}}. \quad (1)$$

Here  $\rho$  is the density,  $V_x$  and  $V_y$  are the Cartesian components of velocity, Fig. 1, and  $\dot{m}$  is the mass flow rate per unit width. The mean (mass averaged) values of the tangential and the axial velocity components,

$$\bar{V}_y(x) = \frac{\int_{y_s}^{y_p} \rho V_x V_y dy}{\int_{y_s}^{y_p} \rho V_x dy}, \quad \bar{V}_x(x) = \frac{\int_{y_s}^{y_p} \rho V_x^2 dy}{\int_{y_s}^{y_p} \rho V_x dy}, \quad (2)$$

are calculated from the numerical results for the cascade flow, Fig. 2. The value for the mean axial velocity component of the flow at the entrance to the cascade,  $\bar{V}_{x1}$ , is known for the design conditions. Therefore, the flow angle,  $\tan \beta = \bar{V}_y(x) / \bar{V}_{x1}$ , and the prescribed angle,  $\tan \beta_p = \bar{V}_{yp}(x) / \bar{V}_{xp1}$ , are determined. For a given  $\bar{V}_{yp}(x)$  the camber line angle  $\theta$  is obtained iteratively from

$$\begin{aligned} \left( \frac{dy_{cl}}{dx} \right)^{N+1} &= \tan \theta^{N+1} \\ &= K^{(p)} \left[ \frac{\bar{V}_{yp}(x)}{\bar{V}_{xp1}} - \left( \left( \frac{\bar{V}_y(x)}{\bar{V}_{x1}} \right)^N - \tan \theta^N \right) \right] \\ &\quad + (1 - K^{(p)}) \tan \theta^N, \end{aligned} \quad (3)$$

where the superscript  $N$  denotes the design iteration number. Occasionally, numerical instabilities occur for some cases. In order to avoid this, the values obtained from Eq. 3 are smoothed by means of a polynomial interpolation to achieve consistent variation of the parameters that could otherwise impair the convergence rate. The relaxation constant  $K^{(p)}$  usually ranges between 0.2 and 0.6. The better the initial camber-line approximation is, the faster the method converges. The initial approximation is calculated from the axial distribution of the mean tangential velocity component and from the flow angle at the entrance. For the initial geometry we adopt a linear variation for  $dy_{cl}/dx$ . This ranges between  $\tan \beta_1 = \bar{V}_{y1} / \bar{V}_{x1}$ , at the leading edge, and  $\tan \beta_2 =$

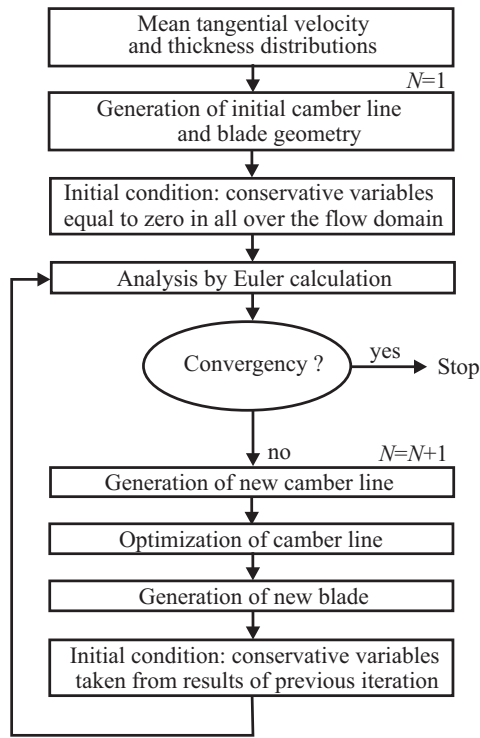


Figure 2 : Iterative inverse method.

$\bar{V}_{y2}/\bar{V}_{x2}$ , at the trailing edge. Here the mean axial velocity component  $\bar{V}_{x2}$  is calculated from the values of  $m$  and  $\bar{V}_{y2}$ , imposed downstream of the cascade, assuming isentropic flow. The exit flow angle is initially unknown, because the mean axial velocity distribution at design conditions,  $\bar{V}_{xp}(x)$ , is a result of the calculation. This velocity distribution is then estimated from mass conservation  $\rho\bar{V}_{xp}(x) = \text{constant}$ . It should be noticed that the stagnation pressure, the temperature and the flow angle are known at the entrance. Design convergence criterion consists in the maximum variation in the camber-line ordinates,  $\Phi_p = \max(y_{cl}^{N+1} - y_{cl}^N)/y_{cl}^N$ , being less than 1%.

### 3 Euler solver

In the absence of external forces and heat conduction, the two-dimensional inviscid flow, in an infinitesimal element, fixed in space, can be described by the system of the Euler equations:

$$\frac{\partial \mathbf{U}}{\partial t} + \frac{\partial \mathbf{F}}{\partial x} + \frac{\partial \mathbf{G}}{\partial y} = 0 \quad (4)$$

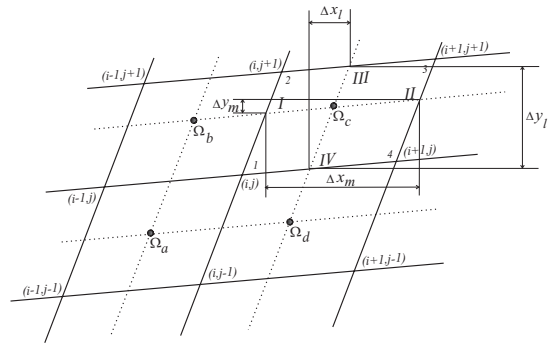


Figure 3 : Mesh and control volume  $\Omega_c$ .

$$\mathbf{U} = \begin{Bmatrix} \rho \\ \rho V_x \\ \rho V_y \\ \rho E \end{Bmatrix}, \mathbf{F} = \begin{Bmatrix} \rho V_x \\ \rho V_x^2 + p \\ \rho V_x V_y \\ \rho V_x H \end{Bmatrix}, \mathbf{G} = \begin{Bmatrix} \rho V_y \\ \rho V_x V_y \\ \rho V_y^2 + p \\ \rho V_y H \end{Bmatrix} \quad (5)$$

Here  $\mathbf{U}$  represents the specific conservative variables per unit volume, mass, momentum and energy.  $\mathbf{F}$  and  $\mathbf{G}$  are the convective fluxes in the  $x$  and the  $y$  directions, in a Cartesian coordinate system, Fig. 1,  $E$  is the stagnation specific energy and  $H = E + p/\rho$  is the stagnation specific enthalpy. For steady flow the energy equation reduces to  $H = \text{constant}$  all over the domain. Considerable benefits are achieved in terms of efficiency and simplicity of the method by assuming that  $H = \text{constant}$  during the time-marching calculation. By doing this, the evolution of the solution loses its physical significance in transient flow. The pressure is given by  $p = (\gamma - 1)\rho [E - (V_x^2 + V_y^2)/2]$ . Our improved numerical model is based on the Ni's variant of the Lax-Wendroff single step method, see [Páscoa, Mendes, and Gato (2002)]. This variant makes use of a finite volume discretization in which two superposed meshes are considered, as shown in Fig. 3.

The primary mesh has its nodes in points 1-2-3-4, with reference to which the values of the variables are stored. The secondary mesh has its vertices  $a-b-c-d$  in the center of the previous volumes. The solution is obtained by marching in time with

$$\mathbf{U}_{i,j}^{n+1} - \mathbf{U}_{i,j}^n = \Delta \mathbf{U}_{i,j} \cong -\frac{\Delta t}{\Omega_{i,j}} \left[ \int_{\Omega_{i,j}} (-\mathbf{F}dy + \mathbf{G}dx) + \frac{1}{2} \int_{\Omega_{i,j}} (-\Delta \mathbf{F}dy + \Delta \mathbf{G}dx) \right]^n \quad (6)$$

In this method, the first term on the right-hand side (r.h.s.) of Eq. 6 is determined by

$$\begin{aligned} & \frac{\Delta t}{\Omega_{i,j}} \int_{\Omega_{i,j}} (-\mathbf{F}dy + \mathbf{G}dx) \\ & = \frac{1}{4\Omega_{i,j}} (\Omega_a \overline{\Delta \mathbf{U}}_a + \Omega_b \overline{\Delta \mathbf{U}}_b + \Omega_c \overline{\Delta \mathbf{U}}_c + \Omega_d \overline{\Delta \mathbf{U}}_d) \end{aligned} \quad (7)$$

Defining  $\Delta x_{21} = x_2 - x_1$  and  $\Delta \mathbf{F}_{12} = \mathbf{F}_1 + \mathbf{F}_2$ , the terms on the r.h.s of Eq. 7 are evaluated as

$$\begin{aligned} & \overline{\Delta \mathbf{U}}_a \frac{\Omega_a}{\Delta t} \\ & = ((\Delta \mathbf{F}_{12} \Delta y_{21} - \mathbf{G}_{12} \Delta x_{21}) + (\mathbf{F}_{23} \Delta y_{32} - \mathbf{G}_{23} \Delta x_{32}) \\ & \quad + (\mathbf{F}_{34} \Delta y_{43} - \mathbf{G}_{34} \Delta x_{43}) + (\mathbf{F}_{41} \Delta y_{14} - \mathbf{G}_{41} \Delta x_{14})) / 2. \end{aligned} \quad (8)$$

The second term on the r.h.s. of Eq. 6 is calculated from:

$$\begin{aligned} \overline{\Delta \mathbf{f}}_c & = \frac{\Delta t}{\Omega_c} [-\overline{\Delta \mathbf{F}}_c (-\Delta y_{lc}) + \overline{\Delta \mathbf{G}}_c (-\Delta x_{lc})], \\ \overline{\Delta \mathbf{g}}_c & = \frac{\Delta t}{\Omega_c} [\overline{\Delta \mathbf{F}}_c (-\Delta y_{mc}) - \overline{\Delta \mathbf{G}}_c (-\Delta x_{mc})] \end{aligned} \quad (9)$$

Assuming that the elements of the surrounding volumes  $a$ ,  $b$ ,  $c$  and  $d$  have approximately equal volumes, we rewrite Eq. 6 as

$$\begin{aligned} \Delta \mathbf{U}_{i,j} & = [(\overline{\Delta \mathbf{U}}_a + \overline{\Delta \mathbf{f}}_a + \overline{\Delta \mathbf{g}}_a) + (\overline{\Delta \mathbf{U}}_b + \overline{\Delta \mathbf{f}}_b - \overline{\Delta \mathbf{g}}_b) \\ & \quad + (\overline{\Delta \mathbf{U}}_c - \overline{\Delta \mathbf{f}}_c - \overline{\Delta \mathbf{g}}_c) + (\overline{\Delta \mathbf{U}}_d - \overline{\Delta \mathbf{f}}_d + \overline{\Delta \mathbf{g}}_d)] / 4 \end{aligned} \quad (10)$$

To increase the computational efficiency, the different terms of Eq. 9 are determined taking

$$\overline{\Delta \mathbf{U}} = \begin{bmatrix} \Delta \rho \\ \Delta(\rho V_x) \\ \Delta(\rho V_y) \end{bmatrix}, \quad (11)$$

$$\overline{\Delta \mathbf{F}} = \begin{bmatrix} \Delta(\rho V_x) \\ V_x \Delta(\rho V_x) + V_x(\rho \Delta V_x) + \Delta p \\ V_y \Delta(\rho V_x) + V_x(\rho \Delta V_y) \end{bmatrix}, \quad (12)$$

$$\overline{\Delta \mathbf{G}} = \begin{bmatrix} \Delta(\rho V_y) \\ V_x \Delta(\rho V_y) + V_y(\rho \Delta V_x) \\ V_y \Delta(\rho V_y) + V_y(\rho \Delta V_y) + \Delta p \end{bmatrix}, \quad (13)$$

$$\begin{aligned} \Delta p & = \left( \frac{\gamma-1}{\gamma} \right) \\ & \quad \times \left[ \Delta \rho H - \frac{1}{2} (V_x \Delta \rho V_x + V_y \Delta \rho V_y + V_x \rho \Delta V_x + V_y \rho \Delta V_y) \right], \end{aligned} \quad (14)$$

$$\rho \Delta V_x = \Delta(\rho V_x) - V_x \Delta \rho, \quad (15)$$

$$\rho \Delta V_y = \Delta(\rho V_y) - V_y \Delta \rho. \quad (16)$$

The corrections to variables given by Eq. 8 are calculated using Eq. 11, 12 and 13. The local time step is limited by the Courant condition.

Numerical algorithms for the solution of the Euler system of equations need to contain a certain level of numerical dissipation. This can be explicitly added to an intrinsically non dissipative numerical scheme, or naturally occur due to the kind of spatial discretization, as generally found in the upwind schemes, see [Henriques and Gato (2002, 2004)]. In the present case a dissipative term is added to the r.h.s. of Eq. 4,

$$\mathbf{D}_{i,j} = \left( \mathbf{d}_{i+\frac{1}{2},j} - \mathbf{d}_{i-\frac{1}{2},j} \right) + \left( \mathbf{d}_{i,j+\frac{1}{2}} - \mathbf{d}_{i,j-\frac{1}{2}} \right), \quad (17)$$

where the term associated to the  $i$  direction is given by

$$\begin{aligned} \mathbf{d}_{i+\frac{1}{2},j} & = \left[ \lambda_{i+\frac{1}{2},j} \cdot \boldsymbol{\varepsilon}_{i+\frac{1}{2},j}^{(2)} \right] (\mathbf{U}_{i+1,j} - \mathbf{U}_{i,j}) - \\ & \quad \left[ \lambda_{i+\frac{1}{2},j} \cdot \boldsymbol{\varepsilon}_{i+\frac{1}{2},j}^{(4)} \right] (\mathbf{U}_{i+2,j} - 3\mathbf{U}_{i+1,j} + 3\mathbf{U}_{i,j} - \mathbf{U}_{i-1,j}) \end{aligned} \quad (18)$$

The remaining terms of Eq. 17 are obtained in an analogous way. The Jacobean flux matrix is scaled using the maximum value of the spectral radius of  $\mathbf{F}$  and  $\mathbf{G}$ ,

$\lambda_{i+\frac{1}{2},j} = \frac{1}{2} \left[ (\lambda_l)_{i,j} + (\lambda_l)_{i+1,j} + (\lambda_m)_{i,j} + (\lambda_m)_{i+1,j} \right]$ , where  $\lambda_l = |u \Delta y_m - v \Delta x_m| + c \Delta m$  and  $\lambda_m = |v \Delta x_l - u \Delta y_l| + c \Delta l$ . The coefficients  $\boldsymbol{\varepsilon}^{(2)}$  and  $\boldsymbol{\varepsilon}^{(4)}$  take values that depend on the existence of flow discontinuities in the neighborhood of the computational cell, as given by

$$v_i = \frac{|p_{i+1} - 2p_i + p_{i-1}|}{(1 - \varepsilon)(|p_{i+1} - p_i| + |p_i - p_{i-1}|) + \varepsilon L_P}, \quad (19)$$

where  $L_P = p_{i+1} + p_i + p_{i-1}$ . This parameter was derived from the van Leer's limiter and has a switching effect, see [Turkel and Jorgenson (1993)], for its theoretical derivation, and [Páscoa, Mendes, and Gato (2002)], for the corresponding numerical implementation. Here  $\varepsilon$  is chosen automatically as a function of shock strength,

$$\varepsilon = \frac{\min(p_{i-2}, p_{i-1}, p_i, p_{i+1}, p_{i+2})}{\max(p_{i-2}, p_{i-1}, p_i, p_{i+1}, p_{i+2})}^\sigma, \quad (20)$$

where  $\sigma$  is as a free parameter. A reasonable range for  $\sigma$  is [0.5, 1]. Furthermore, we need to define

$$\boldsymbol{\varepsilon}_{i+\frac{1}{2},j}^{(4)} = \max \left[ 0, \left( K^{(4)} - \boldsymbol{\varepsilon}_{i+\frac{1}{2},j}^{(2)} \right) \right], \quad (21)$$

$$\boldsymbol{\varepsilon}_{i+\frac{1}{2},j}^{(2)} = K^{(2)} \max (v_{i-1,j}, v_{i,j}, v_{i+1,j}, v_{i+2,j}). \quad (22)$$

The constants  $K^{(2)} = 0.25$  and  $K^{(4)} = 0.0001$  are specified by the user.

In the analysis mode, the inlet boundary conditions for subsonic flow are the stagnation pressure, the stagnation temperature and the flow angle. The exit boundary condition for subsonic flow is the static pressure. The remaining boundary conditions are obtained from the characteristic function theory: the values at the boundary are calculated from the values inside the domain. The slip condition is imposed on the solid boundaries and the periodicity is observed along the periodic boundary.

#### 4 Numerical results

Results presented in [Páscoa, Mendes, and Gato (2002)] validated the described flow analysis algorithm and demonstrated the ability of the method to compute transonic flows with strong shock waves. The above studies also suggested that the method is robust enough to be used in the iterative design of highly loaded (large deflection) turbomachinery blade cascades.

##### 4.1 Consistency evaluation on a parabolic cascade

The consistency of the method was first checked by recovering a given cascade geometry. The test was done considering a parabolic cascade with the blade thickness distribution  $y_{th} = \pm 0.326(x(1-x))^2$  and the blade camber line  $y_{cl} = 0.3(x(1-x))^{1.4}$ , see [Ahmadi and Ghaly (1997)]. The pitch-to-chord ratio is 0.5. The specified conditions are the inlet flow Mach number,  $M_{-\infty} = 0.5$ , and the inlet flow angle,  $\alpha_{-\infty} = 5.5^\circ$ . Calculations were performed using an H-type mesh with  $20 \times 80$  nodes, 40 of them on the blade surface. The analysis code was first used to compute the  $\bar{V}_y$  distribution along the cascade, considering the above geometry and the prescribed flow conditions, see Fig. 4. Next, the inverse method was able to recover the original cascade geometry by starting the calculation with a wrong blade camber line geometry, Fig. 5, and specifying the calculated distribution for  $\bar{V}_y$ , together with the blade thickness distribution. The asymptotic convergence behavior of the camber line during the design iterations is observed in Fig. 5. Results plotted in Fig. 4 show good agreement between the specified  $\bar{V}_y$  distribution for the design and that calculated in the last design iteration. Convergence of the design method is also shown in Fig. 6 that compares the original blade section with the blade section calculated by the in-

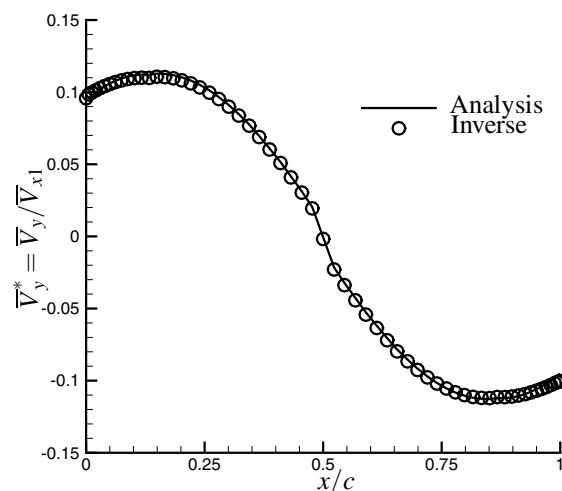


**Figure 4** : Parabolic cascade: non-dimensional mean tangential velocity distributions as a function of the axial coordinate calculated in the analysis (solid line) and in the design (symbols) modes.

verse method. Convergence was achieved after 13 design iterations, when the maximum relative camber-line variation  $\Phi_p$  was less than 1%, see Fig. 7. The algorithm was programmed in FORTRAN and the redesign took around 23 minutes running in a 2 GHz Pentium IV processor.

##### 4.2 Redesign of a transonic compressor cascade.

This test case considers the Sanz's supercritical compressor cascade reported in [Denton, Hirsch, and Meauzé (1990)]. The original compressor cascade was obtained by the hodograph method. The inlet Mach number and the inlet flow angle are  $M_{-\infty} = 0.711$  and  $\alpha_{-\infty} = 30.81^\circ$ , respectively. The exit flow angle is  $\alpha_{+\infty} = -0.35^\circ$ , thus giving an overall design flow turning of  $31.16^\circ$ . The pitch-to-chord ratio is 1.034. The present Euler code was first used to analyze the flow through the compressor cascade. Like in the results of other Euler calculations [Léonard (1992)], the present numerical results do not completely recover the hodograph supercritical solution and show the presence of a shock wave at about 35% of the chord, Fig. 8.

The above design methodology was then applied to demonstrate the ability of the inverse method to produce a new blade camber-line section such that the flow shock-wave is eliminated, when assuming the same design conditions, i.e. overall deflection and load. To illustrate the capabilities of the above design method, a symmet-

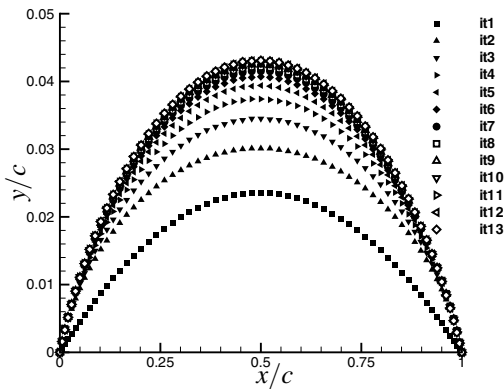


**Figure 5** : Parabolic cascade: evolution of the blade camber line during the design iterations.

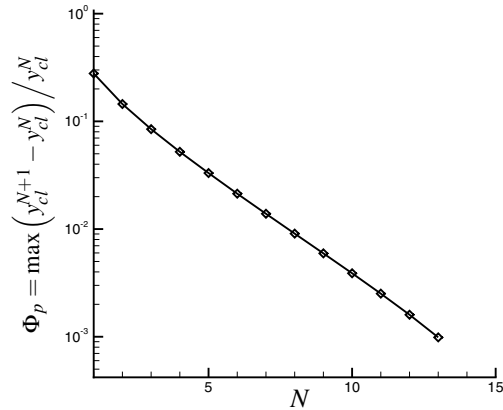


**Figure 7** : Convergence history for the redesigned parabolic cascade.

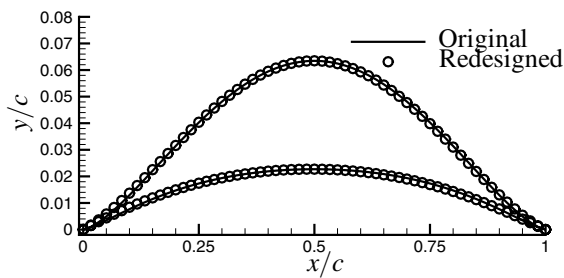


**Figure 6** : Parabolic cascade: original (solid line) and redesigned (symbols) blade geometry.

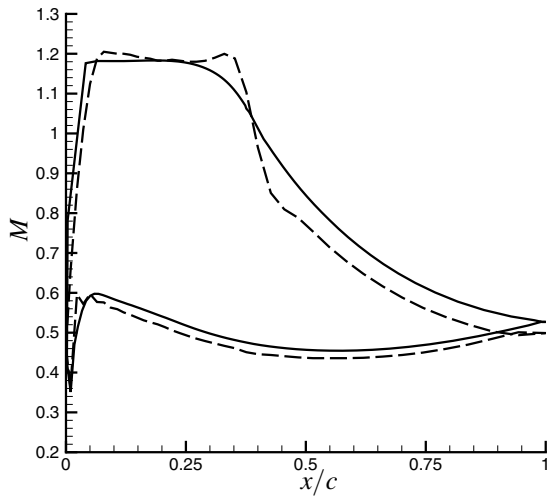
ric fourth-order-polynomial blade-load axial distribution  $g(x)$  was considered for the new design, Fig. 10. This load distribution was imposed by specifying the mean tangential velocity distribution along the  $x$  direction (see Eq. 1), Fig. 1. The values of  $\bar{V}_{y2}$  and  $\bar{V}_{y1}$  were calculated from the above blade design conditions. The imposed mean tangential velocity distribution is plotted in Fig. 9 as a solid line. Also shown in Fig. 9 are the  $\bar{V}_y$  distributions obtained in the flow analysis of the original geometry and in the last design iteration, respectively. The non-dimensional pressure load for the original cascade exhibits a sharp drop due to the presence of the shock-wave, Fig. 10. The imposed load distribution is almost achieved for the redesigned blade, except near sonic conditions where the analysis method introduces small oscillations. The calculations were performed using an H-type mesh with  $160 \times 80$  nodes.

Fig. 11 presents the geometry and the stagnation pressure loss contours,  $\Pi = 1 - p_0/p_{01}$ , for the original and the redesigned blade geometries, respectively. Results plotted in Fig. 11 clearly show that the flow through the redesigned cascade presents lower numerically produced stagnation pressure-loss levels, as could be expected from the analysis of the Mach number distributions plotted in Fig. 12. In fact, for the above flow conditions, the results of the Euler calculation predict the occurrence of a strong shock-wave that extends along the inter-blade channel of the original cascade. In spite of the geometric modification of the compressor blade, the design conditions for the overall deflection is kept, resulting in an exit flow angle of  $\alpha_{+\infty} = -0.36^\circ$  in the last design iteration.

## 5 Conclusions

The paper describes an improved inverse-design two-dimensional method for turbomachinery blading based on the iterative use of an analysis code. The design variables are the mean tangential velocity and the blade thickness distributions along the axial direction. The former gives direct control to the designer over the aerodynamic load distribution on the blade surface, whereas the latter allows the designer to take the stress issue into account before starting the aerodynamic design.

Two test cases were presented to validate the design method. The first was a consistency analysis that showed



**Figure 8 :** Compressor blade cascade: Sanz's hodograph solution (solid line) and present Euler solution (dashed line) for the Mach number distribution on the blade surface.

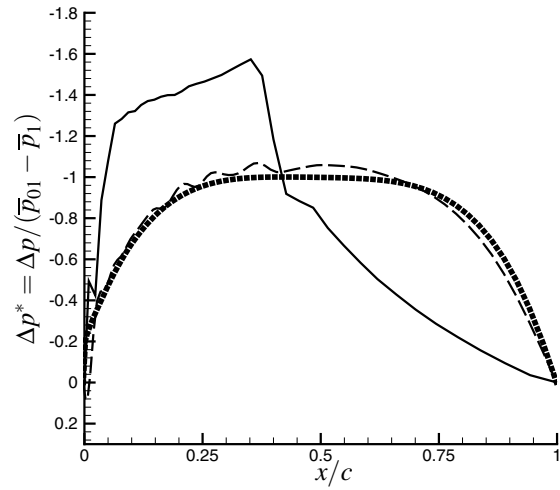


**Figure 10 :** Compressor blade cascade: non-dimensional pressure load prescribed in the design (dotted line, Eq. 1), calculated for the original (solid line) and the redesigned (dashed line) blade geometries.

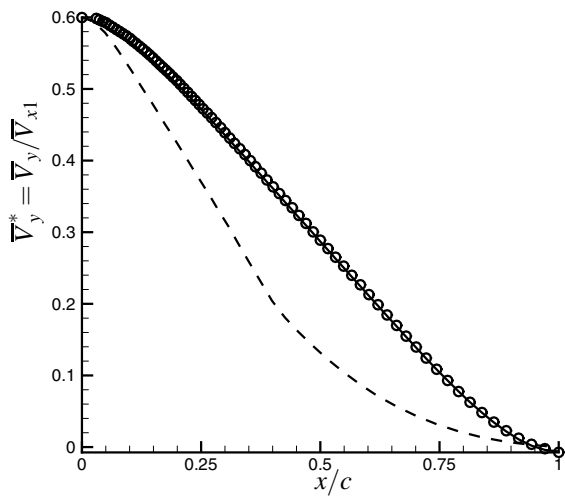


**Figure 9 :** Compressor blade cascade: prescribed (solid line), original (dashed line) and final (symbols) non-dimensional mean tangential velocity distributions as a function of the axial coordinate.

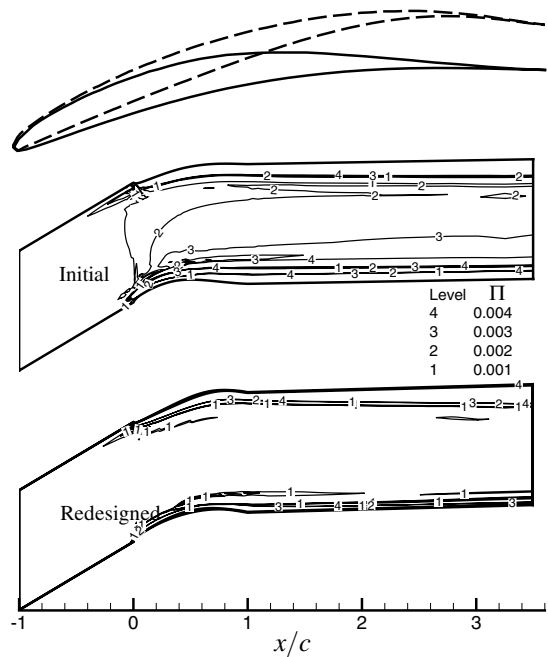


**Figure 11 :** Compressor blade cascade: stagnation pressure loss contours for the original (solid line) and redesigned (dashed line) blade geometries.

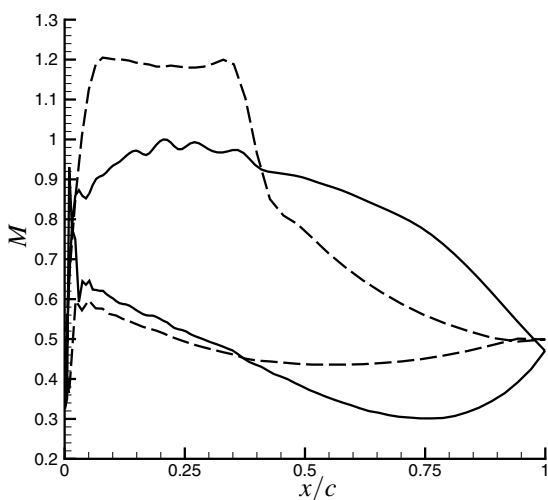


**Figure 12** : Compressor blade cascade: Mach number distributions on the blade surface for the original (dashed line) and redesigned (solid line) blade geometries.

the ability of the method in recovering a parabolic cascade of blades. The second test case considered the redesign of the Sanz's supercritical compressor cascade, originally calculated by the hodograph method. The inverse method was successful in redesigning the compressor cascade, resulting in a new blade camber-line, and blade stagger, for which the Euler calculation predicts a smooth blade pressure-loading distribution, and the elimination of the shock-wave earlier predicted for the original cascade, when assuming the same design conditions in both cases.

The inverse method here presented is planned to be extended to three-dimensions by further specifying the blade stacking line and the mean-swirl distribution along the leading and trailing edges of the blade row.

**Acknowledgement:** This work was partially funded by UBI, IDMEC/IST, and the Portuguese Foundation for Science and Technology, with the support of the European Regional Development Fund, under contract POCTI/EME/39717/01.

## References

**Ahmadi, M.; Ghaly, W. S.** (1997): Aerodynamic design of turbomachinery cascades using a finite volume method on unstructured meshes. In *Proceedings of the*

*Computational Fluid Dynamics '97*. CERCA, Montreal, Canada.

**Atluri, S. N.; Shen, S. P.** (2002): The Meshless Local Petrov-Galerkin (MLPG) Method: A Simple & Less-costly Alternative to the Finite Element and Boundary Element Methods. *CMES: Computer Modeling in Engineering & Sciences*, vol. 3, no. 1, pp. 11–52.

**Atluri, S. N.; Zhu, T.** (1998): A New Meshless Local Petrov-Galerkin (MLPG) Approach in Computational Mechanics. *Computational Mechanics*, vol. 22, pp. 117–127.

**Borges, J. E. T.** (1990): A Three-dimensional Inverse Method for Turbomachinery: Part 1. *ASME Journal of Turbomachinery*, vol. 112, pp. 346–354.

**Borges, J. E. T.; Gato, L. M. C.; Pereira, R. M. R. J.** (1996): Iterative Use of a Time-marching Code for Designing Turbomachine Blade Rows. *Computers & Fluids*, vol. 25, pp. 197–216.

**Burguburu, S.; Toussaint, C.; Bonhomme, C.; Leroy, G.** (2004): Numerical Optimization of Turbomachinery Bladings. *ASME Journal of Turbomachinery*, vol. 126, pp. 91–100.

**Dang, T.** (1995): Inverse method for turbomachinery blades using shock-capturing techniques. *AIAA Paper* 95-2465.

**Dang, T.; Isgro, V.** (1995): Euler-based Inverse Method for Turbomachinery Blades Part 1: Two Dimensional Cascades. *AIAA Journal*, vol. 33, pp. 2309–2315.

**Demeulenaere, A.; Leonard, O.; van den Braembussche, R.** (1997): A Two-dimensional Navier-Stokes Inverse Solver for Compressor and Turbine Blade Design. *Proceedings of the Institute of Mechanical Engineers, Part A*, vol. 211, pp. 299–307.

**Demeulenaere, A.; van den Braembussche, R.** (1998): Three-dimensional Inverse Method for Turbomachinery Blading Design. *ASME Journal of Turbomachinery*, vol. 120, pp. 247–255.

**Denton, J. D.; Hirsch, C.; Meauzé, G.** (1990): Test case a/ca-1 sanz supercritical compressor cascade. In *Test Cases for Computation of Internal Flows in Aero Engine Components*. AGARD-AR-275, France.

**Henriques, J. C. C.; Gato, L. M. C.** (2002): Use of an Euler Solver to Study the Occurrence of Transonic Flow in Wells Turbine Rotor Blades. *Computational Mechanics*, vol. 29, no. 9, pp. 243–253.

- Henriques, J. C. C.; Gato, L. M. C.** (2004): A Multi-Dimensional Upwind Matrix Distribution Scheme for Conservative Laws. *Computers & Fluids*, vol. 33, no. 5-6, pp. 755–769.
- Köller, U.; Mönig, R.; Küsters, B.; Schreiber, H.-A.** (2000): Development of Advanced Compressor Airfoils for Heavy-Duty Gas Turbines — Part I: Design and Optimization. *ASME Journal of Turbomachinery*, vol. 122, pp. 397–405.
- Léonard, O.** (1992): *Conception et Développement D'Une Methode Inverse de Type Euler et Application a la Generation de Grilles D'aubes Transsoniques*. PhD thesis, von Karman Institut for Fluid Dynamics, 1992.
- Levin, O.; Shyy, W.** (2001): Optimization of a Low Reynolds Number Airfoil with Flexible Membrane. *CMES: Computer Modeling in Engineering & Sciences*, vol. 2, no. 4, pp. 523–536.
- Lewis, R. I.** (1982): A method for inverse airfoil and cascade design by surface vorticity. ASME Paper 82-GT-154.
- Nicke, E.; Steinert, W.; Weber, A.; Starken, H.** (1993): Design and analysis of a highly loaded transonic compressor cascade. In *Proceedings of the AGARD Meeting on Technology Requirements for Small Gas Turbines*. AGARD-CP-537, Canada.
- Okumura, H.; Kawahara, M.** (2000): Shape Optimization of Body Located in Incompressible Navier-Stokes Flow Based on Optimal Control Theory. *CMES: Computer Modeling in Engineering & Sciences*, vol. 1, no. 2, pp. 71–77.
- Páscoa, J. C.; Mendes, A. C.; Gato, L. M. C.** (2002): An Efficient Finite Volume Scheme with Improved Artificial Viscosity Suitable for Transonic-flow Calculations. In Rahman, M.; Verhoeven, R.; Brebbia, C. A.(Eds): *International Series on Advances in Fluid Mechanics*, volume 32, pp. 505–514. WIT Press.
- Páscoa, J. C.; Mendes, A. C.; Gato, L. M. C.** (2004): An Inverse Method for Turbomachinery Cascades of Blades — investigation of the existence and uniqueness of solution. In Mendes, A. C.; Rahman, M.; Brebbia, C. A.(Eds): *International Series on Advances in Fluid Mechanics*, volume 40, pp. 3–12. WIT Press.
- Pierret, S.; van den Braembussche, R.** (1998): Turbomachinery blade design using a Navier-Stokes solver and artificial neural network. In *Proceedings of the RTO AVT Symposium on Design Principles and Methods for Aircraft Gas Turbine Engine*. RTO-MP-8, France.
- Rugonyi, S.; Bathe, K. J.** (2001): On Finite Element Analysis of Fluid Flows Fully Coupled with Structural Interactions. *CMES: Computer Modeling in Engineering & Sciences*, vol. 2, no. 2, pp. 195–212.
- Turkel, E.; Jorgenson, P.** (1993): Central Difference TVD Schemes for Time Dependent and Steady State Problems. *Journal of Computational Physics*, vol. 107, pp. 297–308.
- Volpe, G.; Melnik, R. E.** (1981): Role of Constraints in Inverse Design for Transonic Airfoils. *AIAA Journal*, vol. 22, pp. 1770–1778.